Romanian Reports in Physics **72**, 403 (2020)

THE STUDY OF THE PROPERTIES OF WATER DROPLETS USING A MACH-ZEHNDER INTERFEROMETER AND MIE RIGOROUS DIFFRACTION

P. C. LOGOFĂTU, F. GAROI, M. BONI, M. L. PASCU
National Institute for Laser, Plasma and Radiation Physics, P.O. Box MG-36,
RO-077125 Bucharest-Magurele, Romania
E-mails: *petre.logofatu@inflpr.ro; florin.garoi@inflpr.ro;*
mihai.boni@inflpr.ro; mihai.pascu@inflpr.ro

Received July 2, 2019

Abstract. We studied theoretically and experimentally the interference pattern of a water droplet placed in the object arm of a Mach-Zehnder interferometer, and the influence of heating on it. It turns out that due to special circumstances, the diffraction pattern of the sphere in the shadow area is particularly insensitive to changes of the refractive index, because it is identical to the Fresnel diffraction of an opaque disc in the shadow area. However, this pattern is sensitive to changes of the droplet volume caused by dilation, which is another effect of the heating. More promising turns out to be the Mie back- and lateral-scattering. The scattering pattern in this case is sensitive to heating at certain angles. The most general and biggest problem turns out to be the fact that the two effects of heating, the refractive index and radius change, tend to cancel each other. Scanning the scattering angle for sensitivity provides measurement configurations where the two effects of heating do not cancel anymore.

Key words: water droplet, Mach-Zehnder interferometry, Mie rigorous diffraction, Fresnel diffraction, interference pattern sensitivity to heating.

1. INTRODUCTION

The study of water droplets, *i.e.* microfluidics, is driven by the need to use them in technological and biological applications [1, 2]. Optical and laser methods of investigating the droplets are in a privileged position, and they are part of the relatively newly constituted field of optofluidics. In this work the properties of water droplets were studied experimentally and theoretically using interferometry for the express purpose of the determination of temperature changes [3], which causes both refractive index change [4] and dilation [5]. Specifically, we used a Mach-Zehnder interferometer. They were also studied theoretically in the case of a Mie lateral- and back-scattering experimental arrangement [6].

Mie rigorous diffraction [7] had to be used throughout this work; approximations were not good enough.

2. MACH-ZEHNDER INTERFEROMETRY FOR THE WATER DROPLET

2.1. EXPERIMENT AND DATA PROCESSING

We used Mach-Zehnder interferometry in order to determine the changes in temperature of a water droplet. The study was done both theoretically and experimentally. The experimental arrangement is shown in Fig. 1. The droplet is inserted in the object arm of the interferometer. The slant angle α between the wavefronts is controlled through the mirrors. The interferogram is recorded by the sensor. Macrophotography was used for the optical zoom of the interferogram. Except when noted otherwise, the following nominal parameters were used in the calculations: radius $R = 1.061$ mm, wavelength $\lambda = 632.8$ nm (He-Ne laser), refractive index $m = 1.33161$ (corresponding to a temperature $t = 25°$). In Fig. 2 are shown experimentally obtained interferograms and their best theoretical fit.

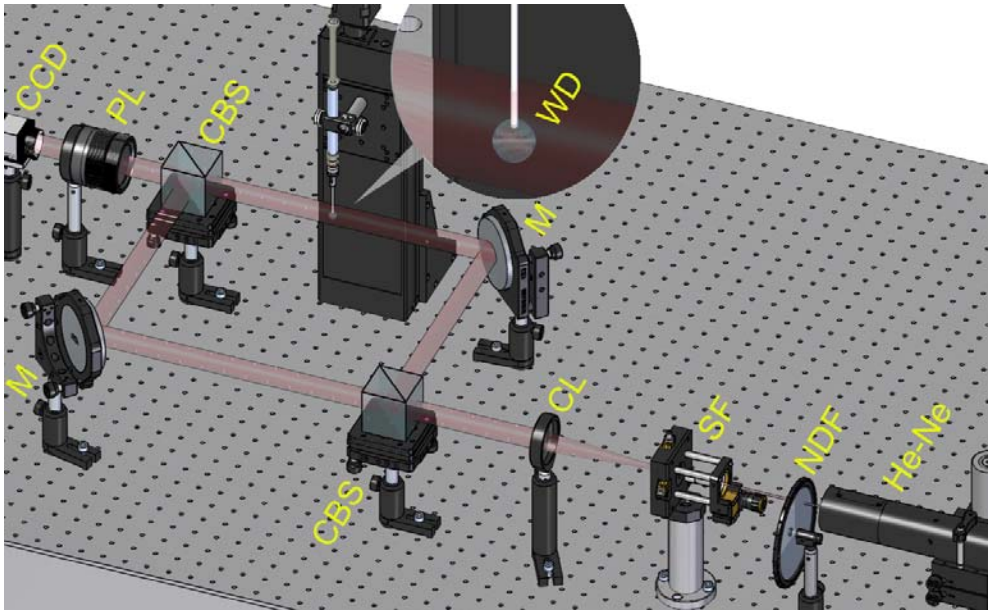

Fig. 1 – Mach-Zehnder interferometer used in this work. The components are the following: CBS – cube beam splitters, SF – spatial filter, NDF – neutral density filter, CL – collimating lens, PL – photo lens, M – mirrors, He-Ne – He-Ne laser, CCD – imaging sensor, and WD – water droplet.

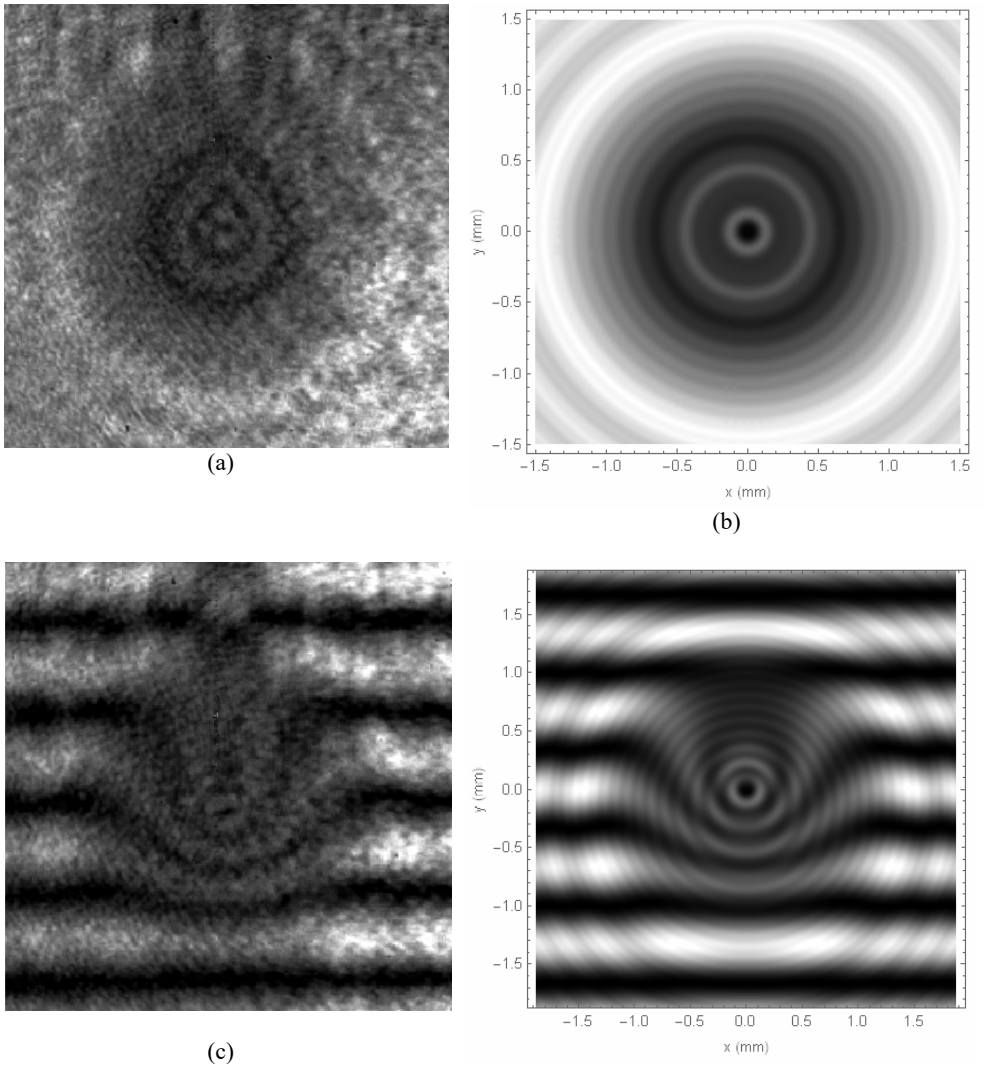

Fig. 2 – Two pairs of experimental interferograms and their best theoretical fit for $\alpha = 0$ rad (a and b) and for $\alpha = 0.95$ mrad (c and d).

For the processing of data, *i.e.* the interferograms, we used Mie rigorous scattering [7]. The geometrical approximation [8] was not good enough in this situation. Fitting the interferograms we obtained a distance $d = 35$ cm from the droplet to the sensor. The slant $\alpha = 0.95$ mrad was also obtained through fitting. It is convenient to decompose the field at the sensor in a radial and a tangential component, because then they are dependent only of one of the components of the Mie scattering, E_θ or E_ϕ:

$$E_{rad}^{tot}(x,y) = \cos\theta\, E_{\theta}(R,m,r,\theta) + \exp(i\,k\,d) + \exp\left(i\,k\left(d-\alpha\, y\right)\right), \tag{1}$$

$$E_{tan}^{tot}(x,y) = E_{\phi}(R,m,r,\theta) + \exp(i\,k\,d) + \exp\left(i\,k\left(d-\alpha\, y\right)\right), \tag{2}$$

where

$$\sin\theta = \sqrt{x^2+y^2}\,/d\,, \tag{3}$$

$$\tan\phi = y/x\,, \tag{4}$$

$$r = d/\cos\theta\,. \tag{5}$$

The idea is to go from the spherical coordinates of the droplet (r, θ and ϕ, the distance from the center of the sphere, the scattering angle and the azimuth), in which the Mie scattered fields are expressed, to the Cartesian coordinates of the sensor (x and y). The sensor coordinates x and y in the shadow area have the values

$$\sqrt{x^2+y^2} \le R. \tag{6}$$

We have a scattering angle $\theta \cong 0$. The distance $d / \cos\theta$ is r, the distance from the center of the sphere to the observation point. It should be mentioned that E_{θ} and E_{ϕ} for small θ and large d are almost identical, in amplitude and phase, and we also have $E_{rad} \cong E_{\theta}$ and $E_{tan} \cong E_{\phi}$. The slant angle α is very small. We assumed unpolarized light. If the light is polarized some simple trigonometric coefficients have to be inserted in Eqs. (1) and (2). In the general case we measure $I = \left(\left|E_{rad}\right|^2 + \left|E_{tan}\right|^2\right)/2$ which is almost equal to any of the intensities corresponding to the fields given in Eqs. (1) or (2).

The analysis of the interferograms showed one thing that is detrimental to our purpose of detecting the heating of the droplet *via* interferometric means. The heating of water has two effects: the decrease of the refractive index m [4] and the increase of the volume [5], specifically the radius R. It turns out the interferogram does not depend at all on m and only very slightly on R. In the next subsection we will explain why this happens.

2.2. FRESNEL DIFFRACTION AND A SUI-GENERIS BABINET PRINCIPLE

In Fig. 3a one can see the Mie diffraction figure due only to the droplet and in Fig. 3b the Mie diffraction figure plus the incident wave from the object arm of the interferometer. The logical continuation of this series is Fig. 2b, the Mie diffraction figure plus the incident wave from the object arm plus the reference wave from the reference arm. Figure 3a cannot be observed physically. There is no physical way to separate the incident wave from the field scattered by the sphere, it is a

mathematical separation done for convenience. However, Fig. 3b is something that can be observed physically and we did; all one has to do in order to obtain it is to block the reference arm of the interferometer. Therefore, the images from Fig. 3 are not interference figures, in particular the observed rings are not circular fringes, as one might be tempted to think.

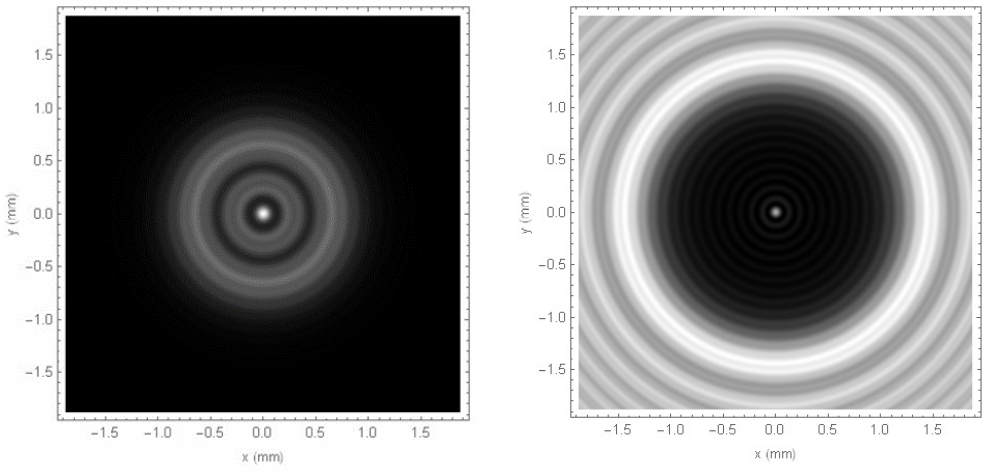

(a) (b)

Fig. 3 – The Mie diffraction figure due to the droplet only (a) and the Mie diffraction figure due to the droplet plus the wave incident on the droplet and with the reference arm blocked (b).

We begin to understand why Fig. 2b is insensitive to changes of m by noticing that Fig. 3a is exactly the Fresnel diffraction figure of an aperture of radius R, on a screen situated at distance d, and Fig. 3b is exactly the Fresnel diffraction figure of an opaque disc of radius R on a screen situated at distance d [9]. Moreover, the diffraction figure corresponds to a Fresnel number $NF = R^2 / \lambda d \cong 5$. The intense luminous point (the Poisson point) in the center is specific to odd Fresnel numbers. Obviously, an aperture and an opaque disc are not characterized by a refractive index. However, they are characterized by a radius, and we do notice some sensitivity of the pattern to changes of R, but it is very small. It is worth mentioning that Fig. 3a and b are connected through the Babinet principle and one may be obtained from the other:

$$E_{aperture} + E_{disc} = E_{incident}. \tag{7}$$

There is a rigorous explanation for the behavior noticed in Fig. 3 and Fig. 2b. See for instance reference [10]. However, we think it would be more helpful an intuitive explanation using the ray tracing in the geometrical approximation, which is illustrated in Fig. 4. We take into consideration only the rays that refract without

internal reflection in the droplet, which represent most of the scattered radiation. One notices that most of the rays are deflected far outside the shadow area of the droplet. Only the rays diffracted around the edges of the droplet contribute to the diffraction figure. Therefore, the droplet acts like an opaque disc, although it is transparent.

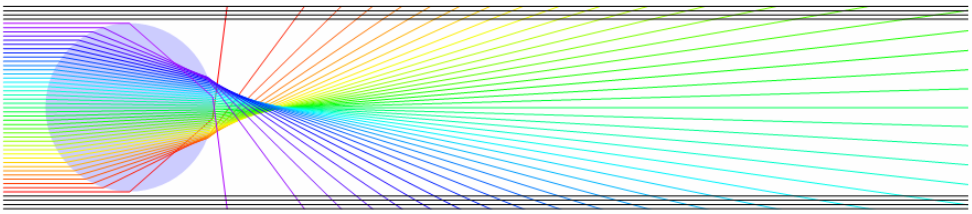

Fig. 4 – Ray tracing for the rays that do not reflect internally in the droplet, they just refract twice. These rays contain by far most of the energy scattered by the sphere.

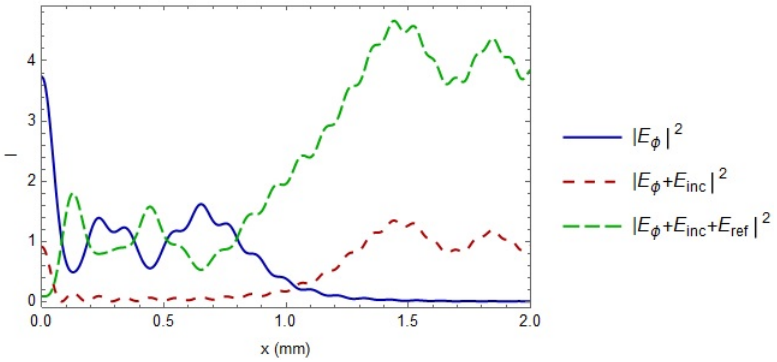

Fig. 5 – Radial section through Fig. 3a, Fig 3b and Fig. 2b. It illustrates how adding the incident wave and the reference wave to the scattered wave a reversal of intensities is obtained.

It is worth mentioning an aspect which does not seem to have a deep physical significance, yet it is remarkable. Namely we were able to formulate a sui-generis Babinet principle in this special case of the interferometry of the sphere. This sui-generis Babinet principle is illustrated in Fig. 5 and consists in a reversal of intensities when one adds to the field scattered by the droplet the incident wave and the reference wave. It takes place because of the particularity that the incident and the reference wave have an amplitude close to the average of the scattered field but of opposite sign. There is a phase difference of π between them. Adding the incident wave has the consequence of making the shadow area dark. Adding the reference wave makes it brighter again, but the intensities are reversed. One can express this phenomenon as

$$I_{scattered} + I_{interference} = 2I_{incident}\,. \tag{8}$$

This sui-generis Babinet principle is for intensities, not for fields, and the sum of the complementary intensities is double the incident intensity.

3. MIE LATERAL- AND BACK-SCATTERING AND SENSITIVITY SCAN

Since the Mach-Zehnder interferometer has low sensitivity to temperature changes, we investigated a simpler experimental arrangement, the Mie lateral-scattering (including back-scattering). We already have some experience with such an experimental arrangement [6]. We scanned the scattering angles in search for optimum sensitivity. It is a theoretical study only.

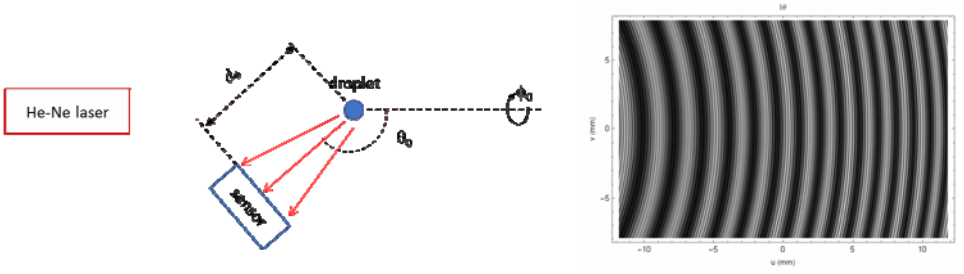

(a) (b)

Fig. 6 – The experimental arrangement for lateral-scattering (a) and simulation of image captured by the sensor (b).

Again, a problem here is to convert the spherical coordinates of Mie scattering into the Cartesian coordinates of the sensor. Also, we need to express the ordinary values θ, ϕ and d in terms of the center values for the scattering angle θ_0, the azimuth ϕ_0 and the distance to the center of the droplet d_0 and the Cartesian coordinates of the sensor u and v. We have

$$I(\theta,\phi,d) = I\left(\theta(\theta_0,d_0,u,v),\phi(\theta_0,d_0,u,v),d(d_0,u,v)\right), \tag{9}$$

where

$$\cos\theta = \frac{d_0\cos\theta_0 + u\sin\theta_0}{\sqrt{{d_0}^2+u^2+v^2}}, \tag{10}$$

$$\tan(\phi_0-\phi) = \cot\phi = \frac{v}{d_0\sin\theta_0 - u\cos\theta_0}, \tag{11}$$

$$d = \sqrt{{d_0}^2+u^2+v^2}\,. \tag{12}$$

In Eqs. (9) and (11) we took into account that in our experimental arrangement we have $\phi_0 = 90°$. The scattered output captured by the sensor looks certainly like an interferogram. There is a carrier wave and a modulation wave and also a curvature of the fringes. Because the fringes are very thin, of the order of microns, the interferogram is very sensitive to vibrations. Also, the output is very weak. These facts can cause experimental difficulties.

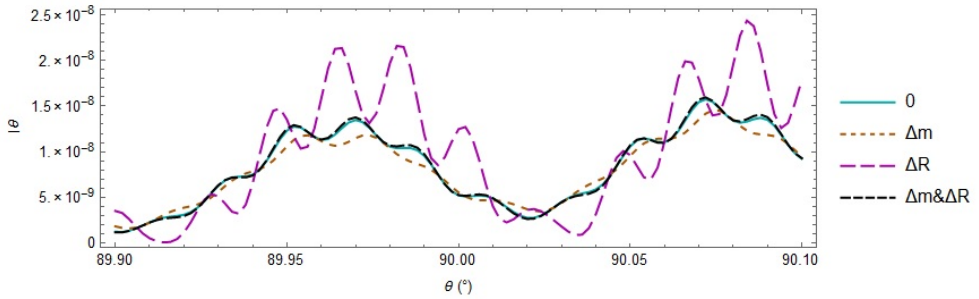

Fig. 7 – Illustration of the compensation of the effect on the output scattered by the droplet of the refractive index and the radius change. They tend to modify the curve in opposite directions. Δm and ΔR correspond to a temperature increase of $\Delta t = 0.01°$ at 25.00°.

The most general and the biggest problem we have to overcome, which affects both scattering measurements and interferometric measurements, is the fact that the two effects caused by the heating on the droplet, the decrease of the refractive index and the dilation, influence the scattered output in opposite ways. Figure 7 illustrates this phenomenon. Apart from the curve corresponding to the original temperature of 25.00° ("0"), we have drawn the curve for a droplet with the decreased refractive index corresponding to the temperatue 25.01° but with the same radius (Δm), the curve for a droplet with the same refractive index but with a increased radius corresponding to 25.01° (ΔR) and the curve corresponding to 25.01° that takes into account both changes (Δm & ΔR). One may notice that very small changes of the refractive index or radius, if they occur alone, change strongly the output. But when they occur together they cancel each other. The curve Δm & ΔR is barely distinguishable form the curve "0".

Therefore we need to optimize the measurement configuration. And we did by scanning the scattering angle θ. We defined a measurement configuration as 101 measurements corresponding to equidistant scattering angles located in a range of 2° around a central scattering angle θ_0. In Fig. 8 is illustrated the ability of an optimized configuration to distinguish between scattering curves corresponding to differences of 0.1°C. We will explain next how this optimum configuration was obtained. For now let us notice that the experimental curve corresponding to a temperature of the droplet of 24.5°, is best fitted by the theoretical curve corresponding to 24.5° and

can be clearly distinguished from the theoretical curves corresponding to 24.4° and 24.6°. A 0.1° discrimination ability of the method is demonstrated.

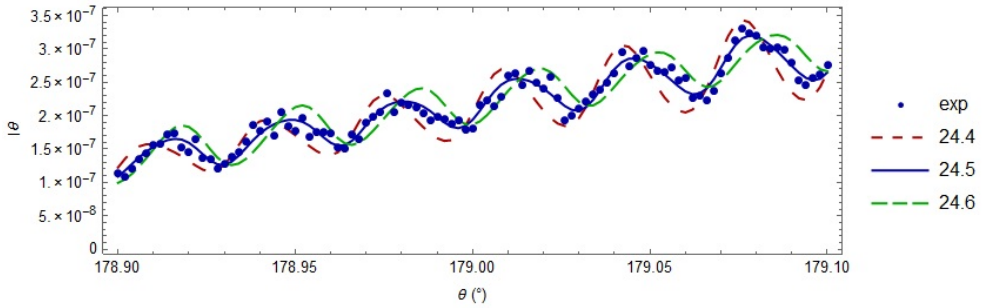

Fig. 8 – Illustration of the fit for the optimum measurement configuration defined by $\theta \in (178.9° \ldots 179.1°)$. The experimental curve, generated by adding white Gaussian noise to the curve corresponding to the temperature of 24.5°, is much better fitted by the theoretical curve for 24.5° than by the theoretical curves for 24.4° and 24.6°.

In Fig. 9 is illustrated the optimization process, *i.e.* the scanning for the optimum scattering angle θ_0. To make the scan possible, we had to define some parameters for the optimization. The parameter used to characterizes the quality of the fit was the function $\Delta\chi^2$:

$$\Delta\chi^2(t) = \sum_{i=1}^{N} \left(\frac{I_{\exp}(\theta_i) - I_{teo}(\theta_i, t)}{\sigma\left(I_{\exp}(\theta_i)\right)} \right)^2 . \tag{13}$$

We notice that in order to use $\Delta\chi^2$ we need to know the experimental measurement error $\sigma(I)$ (see Eq. 14). To determine this parameter we used an euristic function. In choosing the form of the function we were guided by experience with scattering, but also by some euristic principles. We assumed the measurement error should have a term proportional to the measured intensity I, hence the parameter ε. We also assumed the measurement error should have a term proportional to the partial derivate of I on the scattering angle θ, hence the parameter $\delta\theta$. The term δ_0 was added in order to prevent the sensitivity search to go to low intensities.

$$\sigma(I) = \delta_0 + \varepsilon I + \left| \frac{\partial I}{\partial \theta} \right| \delta\theta . \tag{14}$$

We came up with the following values for these terms: $\varepsilon = 10^{-3}$, $\delta_0 = 10^{-9}$ I_{incident} and $\delta\theta = 10^{-6}$. Finally we defined the sensitivity:

$$S = \frac{1}{N} \sum_{i=1}^{N} \frac{2\left|I_i(t_2) - I_i(t_1)\right|}{\sigma\left(I_i(t_1)\right) + \sigma\left(I_i(t_2)\right)} . \tag{15}$$

N is 101, the total number of measurements and the indexes *i* correspond to the scattering angles θ_i which define the measurement configuration.

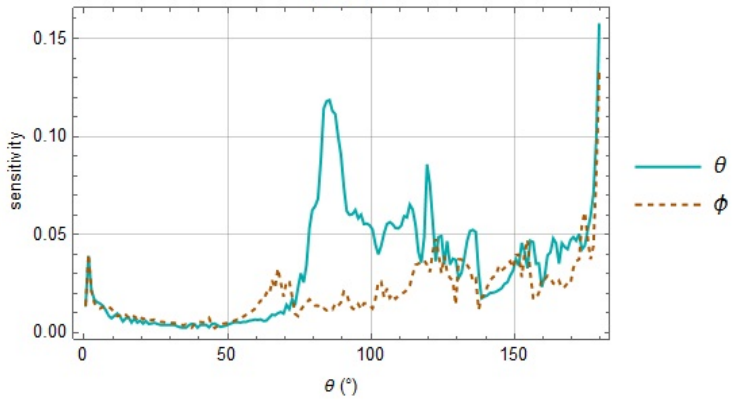

Fig. 9 – Illustration of the sensitivity scan of the experimental configurations for the scattering intensities I_θ and I_ϕ. An experimental configuration is defined by a range of 2° of scattering angles around the center value. In the figure each θ represents such a range of angles.

The end results of the sensitivity scan are shown in Fig. 9. One may notice *S* for I_θ has two maxima, one for back-scattering and another for perpendicular-scattering. *S* for I_ϕ has a maximum only for back-scattering. For Fig. 8 we chose the optimum configuration of I_θ at back-scattering.

4. CONCLUSIONS

The most general and the biggest problem we encountered in trying to determine the change of the temperature of the water droplet was the fact that the change of the refractive index and the dilation tend to compensate each other their effects on the light output scattered by the droplet. An experimental and theoretical study of the Mach-Zehnder interferometry of the water droplet shew that the interference pattern of the droplet in the shadow area is particularly insensitive to changes of refractive index, but it is somewhat sensitive to changes of the radius. The Mach-Zehnder interference pattern is identical to the Fresnel diffraction of an opaque disc in the shadow area. We were able to formulate a sui-generis Babinet principle for the particular case of diffraction in the shadow area, but for the intensities, not for the fields. A simpler Mie scattering experiment without interference seems more promising for our purpose. A theoretical study of such an experiment and the afferent optimization by scanning the scattering angle lead us to the conclusion that that for the Mie back- and perpendicular-scattering the interference pattern is quite sensitive to droplet heating. We anticipate some experimental problems: the scattering output is very low and the fringes are very sensitive to vibrations.

REFERENCES

1. D. Psaltis, S. R. Quake, and C. H. Yang, Nature **442**, 381–386 (2006).
2. V. R. Horowitz, D. D. Awschalom, and S. Pennathur, Lab. Chip. **8**, 1856–1863 (2008).
3. A. R. Glover, S. M. Skippon, and R. D. Boyle, Appl. Opt. **34**, 8409–8421 (1995).
4. A. N. Bashkatov, E. A. Genina, Proc. SPIE **5068**, 393–395 (2003).
5. https://physics.info/expansion/
6. P. C. Logofătu, I. Ardelean, D. Apostol, I. Iordache, M. Bojan, C. Moisescu, and B. Ioniţă, J. Appl. Phys. **103**, 094911 (2008).
7. M. Born and E. Wolf, *Principles of Optics*, Cambridge University Press, Cambridge, 1999.
8. W. J. Glantschnig and S.-H. Chen, Appl. Opt. **20**, 2499–2509 (1981).
9. J. W. Goodman, *Introduction to Fourier optics*, 4th ed, MacMillan, New York, 2017.
10. J. A. Lock and E. A. Hovenac, Am. J. Phys. **61**, 698–707 (1993).